Upper Oceanic Warming in the Gulf of Mexico between 1950 and 2020

Zhankun Wang,[a,b] Tim Boyer,[c] James Reagan,[c] Patrick Hogan[b]

[a] *NOAA's National Centers for Environmental Information, Stennis Space Center, MS, 39529*

[b] *Northern Gulf Institute, Mississippi State University, Stennis Space Center, MS, 39529*

[c] *NOAA's National Centers for Environmental Information, Silver Spring, MD, 20910*

Corresponding author: Zhankun Wang, zhankun.wang@noaa.gov

ABSTRACT

We estimate ocean heat content (OHC) change in the upper 2000 m in the Gulf of Mexico (GOM) from 1950 to 2020 to improve understanding of regional warming. Our estimates are based on 192,890 temperature profiles from the World Ocean Database. Warming occurs at all depths and in most regions except for a small region at northeastern GOM between 200 and 600m. GOM OHC in the upper 2000m increases at a rate of 0.38±0.13 ZJ decade^{-1} between 1970 and 2020, which is equivalent to 1.21±0.41 TeraWatts (TW). The GOM sea surface temperature (SST) increased ~1.0±0.25 ˚C between 1970 and 2020, equivalent to a warming rate of 0.19±0.05 ˚C decade^{-1}. Although SST in the GOM increases at a rate approximately twice that for the global ocean, the full-depth ocean heat storage rate in the GOM (0.86±0.26 W m^{-2}) applied to the entire GOM surface is comparable to that for the global ocean (0.82 to 1.11 W m^{-2}). The upper 1000m layer accounts for approximately 80-90% of the total warming and variations in the upper 2000m in the GOM. The Loop Current advective net heat flux is estimated to be 40.7±6.3 TW through the GOM. A heat budget analysis shows the difference between the advective heat flux and the ocean heat storage rate (1.76±1.36 TW, 1992-2017) can be roughly balanced with the annual net surface heat flux from ECCO (-37.9 TW).

1. Introduction

The ocean heat content (OHC) of the global ocean has increased significantly over the past few decades (Levitus et al. 2012; IPCC 2021). Although oceanic warming is a global phenomenon, its manifestations and consequences are different regionally. Therefore, quantifying warming/cooling trends on a regional scale is critical to understanding the impacts and conducting risk assessments for ecologically and economically significant marginal seas, such as the Gulf of Mexico (GOM). Most oceanic warming research has been focused on a global scale, with some exceptions (e.g. equatorial Indian Ocean, Alory and Meyers 2009; Gulf of Maine, Seidov et al. 2021). Very little research is available regarding detailed spatiotemporal distributions of the warming/cooling in the upper water of the GOM (Ochoa et al. 2021; Li et al. 2022). Temperature profiles have been collected in the GOM since the 1920s and are freely available via the World Ocean Database. In this manuscript, we use the temperature profiles from the World Ocean Database 2018 (WOD18; Boyer et al. 2018) and its updates collected between 1950 and 2020 to quantify the OHC trend in the GOM.

Previous studies on oceanic warming in the GOM are mostly restricted to sea surface temperature (SST) changes (e.g. Glenn et al. 2015; Muller-Karger et al. 2015; Li et al. 2022) and deep-water warming (Ochoa et al. 2021). Glenn et al. (2015) studied the SST warming trend for the Caribbean and surrounding regions (including GOM) between 1982 and 2012 using an optimum-interpolated SST product. They found a regional increase in annual average SST of 0.15 ˚C decade^{-1} for the period 1982-2012 in the Caribbean and Gulf of Mexico, which was larger than the annual global rate of 0.11 ˚C decade^{-1} during the same period. They also indicated that the warming was likely influenced by the El Niño–Southern Oscillation (ENSO) based on cross-correlation analysis. Muller-Karger et al. (2015) found that SST, wind speed, and sea surface height anomaly (SSHA) showed a statistically significant increase between the early 1980s and 2012 in the GOM. The increase in SST anomaly ranged between 0.17 and 0.3 ˚C decade^{-1} in the interior (depth>1000m) GOM. Li et al. (2022) characterized the spatial patterns of the monthly trends in SST of the GOM and investigated the seasonal variations in warming trends using satellite SST between 1982 and 2019. They found that the summer warming trend (0.22 ˚C decade^{-1}) was larger than the winter trend (0.05 ˚C decade^{-1}), suggesting seasonal variations of surface warming in the GOM. Regional datasets for the Florida Keys outer-reef showed 0.8-0.9 ˚C of warming in sea surface temperature over the 20th century and can be fully accounted for by the warming observed from 1975 to 2007 (Kuffner et al. 2015). In a study of Hurricane Harvey, Trenberth et al. (2018) discovered that OHC for the upper 160 m was the highest on record in the GOM prior to the beginning of the summer of 2017, which not only increased the fuel availability for Hurricane Harvey intensification, but also increased flooding rains on land. Ochoa et al. (2021) studied deep-water warming in the western GOM between 2003 and 2019. They found a stable linear warming trend of 0.016±0.002 ˚C decade^{-1} at about 3500 m using near-bottom measurements at four sites between 2007 and 2018 and a rate of approximately 0.018±0.002 ˚C decade^{-1} below 2000m between 2003 and 2019 using CTD data from eight oceanographic cruises. The change of the OHC and the warming/cooling trend in the upper 2000m of the GOM are still unclear. The present study will fill in the gap about the OHC change in the upper 2000m using WOD temperature profiles, which allow us to extend satellite-only analyses backward in time and also allow us to diagnose trends at deeper depths.

Knowing how the warming/cooling trend varies on different spatial and temporal scales is critical for understanding the consequences of oceanic climate change and climate variability

in the GOM. The increased temperature can affect many aspects of the natural environment and ecosystem in the GOM, including coral reefs (Jordán-Dahlgren et al. 2005; Lunden et al. 2014), Atlantic Bluefin tuna (Muhling et al. 2011), and poleward organisms distribution shift (Fodrie et al. 2010). The GOM is a semi-enclosed marginal sea that extends from 17.5 ˚N to 31.5 ˚N latitudes and from -98 ˚W to -80 ˚W. It has a long coastline with ~4.9% of the US population living along the GOM coast (Cohen 2018; McKinney et al. 2021). It forms a complex semi-enclosed system with interactions among physical, biogeochemical, socioeconomic, and human activities. GOM ecosystems are vulnerable to climate change impacts and threatened by habitat degradation, ecosystem fragmentation, and increased population growth along the coast (McKinney et al. 2021).

Estimating and analyzing the OHC is essential for understanding the evolution of the GOM long-term warming/cooling trend. Following Levitus et al. (2012), we use the term "ocean heat content" instead of "ocean heat content anomaly" used in some publications because OHC is always computed with a reference mean subtracted from each observation. In this paper, using OHC estimated from the objectively analyzed pentadal anomaly temperature fields (observations interpolated to standard levels subtracted from the World Ocean Atlas 2009 climatological mean temperature field; Locarnini et al. 2018) from the World Ocean Database (WOD, Boyer et al. 2018), we investigate the spatial and temporal distribution of the OHC change over the past 70 years and quantify the warming trend in the GOM. We further discuss the heat budget closure in the GOM using the net surface heat flux from multiple heat flux products and the estimated Loop Current net advective heat flux.

2. Data and Methods

a. Data

The warming trend in the GOM is quantified using running pentadal (five-year) objectively analyzed gridded temperature anomaly fields. The temperature data used to generate the pentadal gridded fields include 192,890 temperature profiles (Fig. 1) collected between 1948 and 2020 in the WOD 2018 (WOD18; Boyer et al. 2018) and its updates. WOD is the world's largest collection of publicly available ocean profile data. The instrument and platform (vehicle from which the instruments were deployed), years of use, and standard deepest depths of measurement are shown in Table 1.

Reversing thermometers attached to bottles and later Conductivity-Depth-Temperature (CTD) sensors have been deployed in most years from research ships by U. S. universities, mainly those in proximity to the Gulf, notably Texas A&M, the University of Southern Mississippi, Louisiana State University, and the University of Miami. NOAA research ships provide a major contribution of bottle/CTD temperature profiles from research and monitoring programs. There are also contributions from Mexican and Cuban research ships historically. Though not many in overall numbers, bottle and CTD measurements are often full-depth (surface to ocean bottom), calibrated, and of high quality and cover the entire Gulf.

From 1948-1968, Mechanical Bathythermographs (MBT) were the main observing system for subsurface temperature both globally and in the GOM. The MBT data, which could be obtained from a moving ship, were used in weather and climate forecasting and covered the entire Gulf, but only to depths of 125 m. and later ~250 m. MBT temperature profiles were made mainly from research and U. S. Navy ships. The Expendable Bathythermograph (XBT) improved on the MBT in that it could be deployed from a moving ship at normal cruise speed. Ships of Opportunity now included merchant ships and the XBT quickly became the main ocean subsurface observing system in the Gulf. Air drop XBTs (AXBT) were also used in Gulf wide observational experiments in the 1970s, but in more recent years have been limited to hurricane drops. XBTs reached depths of 460 m initially, later 760 m., with some AXBTs and ship based XBTs reaching 1830 m depth.

With the advent of the Argo autonomous profiling float program in 2000 (Wong et al. 2020), XBT deployment was cut back significantly globally and in the Gulf. Some pre-Argo profiling floats were deployed in the Gulf but the Argo program initially focused on the open ocean. Starting in 2010, Argo floats were deployed in the Gulf of Mexico. Argo floats record temperature profiles every 5 or 10 days from 2000 m to the surface. In between, floats drift at 1000 m depth. The coverage of Argo floats is the entire Gulf, excepting the shelf and coastal regions. In addition to Argo floats from the U. S. and Mexican Argo programs, there is a small contribution of ALAMO (Air-Launched Autonomous Micro Observer) profiling floats. Gliders, autonomous remotely controlled ocean vehicles which can make high time and space frequency measurements (Lee and Rudnick, 2018) have been increasingly used in the Gulf since 2010. Gliders flown by Texas A&M and other Gulf proximate U. S. universities, as well as by the U. S. Navy, have provided coverage of the northern half of the Gulf. Many gliders are deployed to explore the mixed-layer, but some dive to 1000m depth.

Overall, the temperature profiles provide over 80% coverage of the entire GOM at the sea surface in most pentadal periods, except for the period between 2006 and 2010 (Figs. 1 and 2). The data density is higher in the northern GOM than the southern GOM in almost all years. The eastern Gulf usually has a larger data density than the western Gulf. All WOD18 temperature profiles are analyzed in a consistent manner by a series of quality control (QC) procedures. The QC includes duplicate elimination, range and gradient checks, statistical checks and subjective flagging, etc. More details on data sources, data quality control, and data processing procedures as well as objective analysis methods can be found in Boyer et al. (2018) and Locarnini et al. (2018).

Years	Instrument/platform	Number of profiles	Depth range
1950-2020	Bottle (reversing thermometer) and Conductivity-Depth-Temperature (CTD) from research ship	43,353	Full depth
1967-2020	Expendable bathythermograph (XBT) from Ship of Opportunity	36,662	460 m, 760m, 1830 m
1948-1994	Mechanical Bathythermograph (MBT) from Ship of Opportunity	27,909	125 m, 250 m
2010-2019	CTD from Glider	71,948	1000 m
1999-2020	CTD from profiling float (mainly Argo)	13,017	2000 m

Table 1. Temperature profiles in the Gulf of Mexico by instrument/platform type

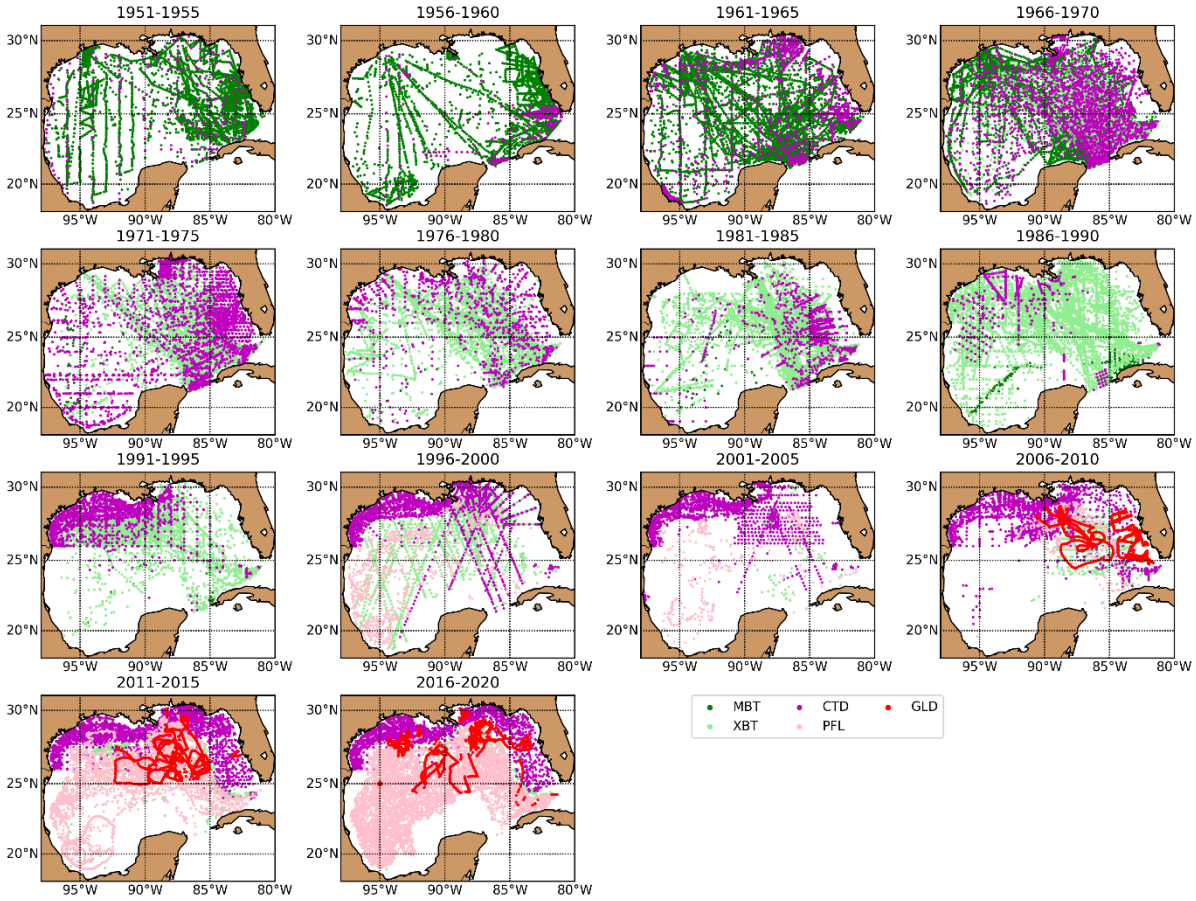

Fig. 1. Temperature profiles' spatial distribution for every pentadal (5-year) period from 1951 to 2020. The color shows different measurement types. MBT: mechanical bathythermograph (MBT) data, digital BT (DBT), and micro-BT (μBT); XBT: expendable bathythermograph and AXBT; CTD: bottle, Conductivity-Temperature-Depth (CTD), expendable CTD (XCTD) data; GLD: glider data; PFL: profiling float data, mainly from the Argo program. Some of the data points may not be shown due to data overlap.

b. Pentadal Objective Analysis

In order to calculate the OHC, the data need to be gridded and gaps need to be filled. We use running pentadal (5-year) objective analysis to create 1˚×1˚ gridded temperature anomaly fields at standard depth levels for running pentad from 1950 to 2020. More about pentadal objective analysis can be found in Levitus et al. (2012). The pentad is used in our analysis to ensure sufficient data distribution. Fig. 2 shows the temperature data coverage in percentage as a function of time (years) and depth (m) for the pentadal running analysis. The percentage coverage is computed based on the 1˚×1˚ gridded number of observations. For any grid at any standard depth, at least one observation is needed to be considered having data. Only data with WOD flag=0 are used. The data coverage is greater than 70% in the upper 100m in all the years between 1950 and 2020 except in the late 2000s. In the upper 750m, the data has

relatively good coverage with a percentage greater than 70% in most years after 1965, primarily due to the usage of XBT, which measures temperature down to the depth of about 760 m from moving ships. Below 760m the coverage is lower except after 2010 when CTD and Argo became the dominant instruments. The hatched areas in Fig. 2 show the percent coverage of less than 30% to mask the low coverage periods.

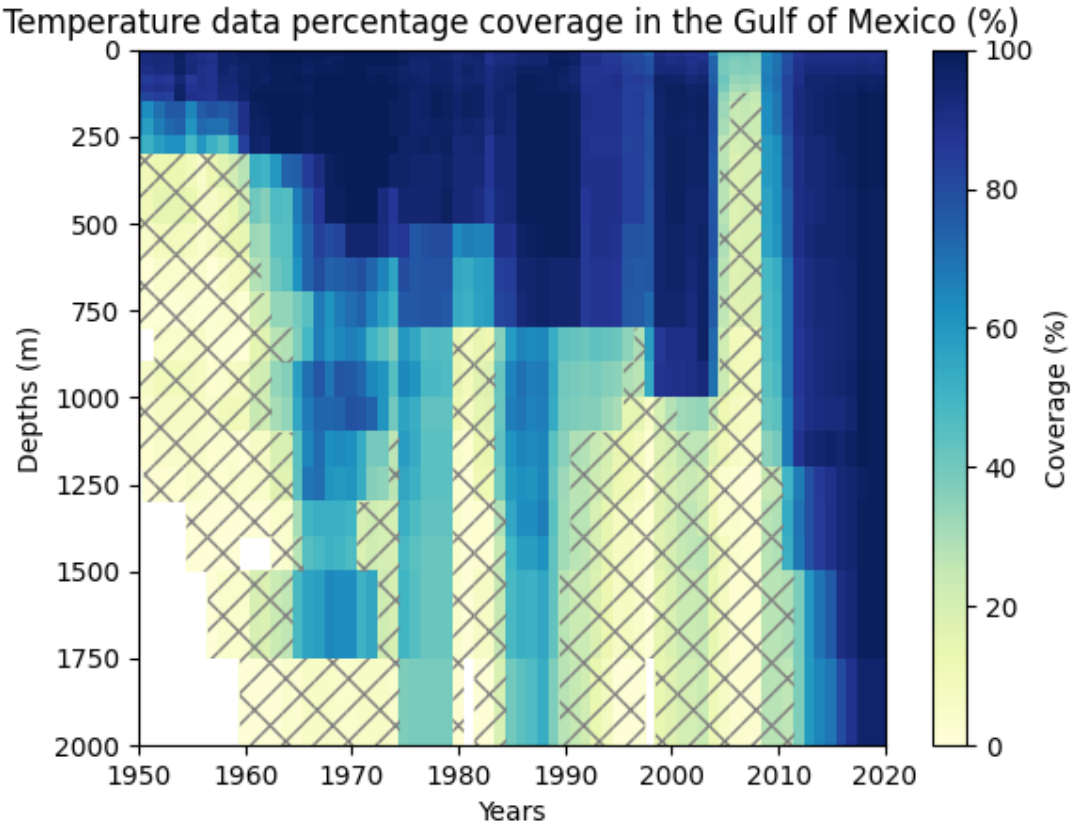

Fig. 2. Percentage of data coverage of one-degree squares with at least one observational profile. Hatched area indicates the percentage of coverage less than 30%.

To obtain temperature anomalies for each 1˚ grid at every standard depth level, we subtract the 1˚ mean temperature from a monthly climatological value. We use the monthly climatological temperature fields from the World Ocean Atlas 2009 (WOA09) as the reference fields. XBT/MBT biases are corrected following Levitus et al. (2009). The same objective analysis procedure as in Locarnini et al. (2018) and Levitus et al. (2012) is applied to these temperature anomaly values to create a gridded objectively analyzed temperature anomaly field for each standard depth level for each year (with 80% overlap). A first-guess field of zero is used for the temperature anomaly objective computations, which is a

conservative estimate by assuming no change from climatological mean. This will underestimate the warming trend in areas and periods with low data coverage (data density). Given the good data coverage shown in Fig. 2, we expect that it is not a large underestimate in the GOM because the first-guess field (zero) remains only there are no data at all within an ~800 km radius (the influence radius of the objective analysis, Levitus et al. 2012). Caution should be taken when examining the results in poor data coverage regions and periods.

c. Ocean Heat Content

Ocean Heat Content (OHC) is based on 1-degree gridded, interpolated temperature anomaly fields T'_w at standard depth levels. The OHC at gridbox [*i,j*] can be estimated as

$$OHC(\mathbf{x};t) = \rho_w c_{pw} \int_{D1}^{D2} T'_w(\mathbf{x},z;t)dz \qquad (1)$$

Where **x** is a horizontal coordinate vector $\mathbf{x} = [i,j]$. $\rho_w = 1026\ kg\ m^{-3}$ is the seawater density, $c_{pw} = 3995\ J\ kg^{-1}\ ℃^{-1}$ is the specific heat capacity of seawater, D1 is the upper depth and D2 is the lower depth. *z* represents depth and *t* is time.

Integrated OHC can be estimated by integrating OHC at each gridbox over area and depth range in a selected region. The warming/cooling rate can then be determined by ocean heat storage rate Q_t, which is defined as the time derivative of OHC (Etter, 1983).

$$Q_t = \frac{\partial OHC}{\partial t} \qquad (2)$$

The OHC analysis for this study was conducted on both basin and grid levels. The linear statistical trend was calculated as OHC change with time using simple linear regression if the p-value was less than 0.05. Linear regression and standard error estimate are conducted using the Python SciPy.stats module. 95% confidence interval is used in the uncertainty estimate. Autocorrelation was tested in the OHC residuals from the regression analysis using Durbin Watson statistic. If autocorrelation needed to be considered, the effective degrees of freedom (effective sampling size) were determined based on the e-folding decay time of autocorrelation (Panofsky and Brier, 1958) and later used to evaluate standard errors and 95% confidence intervals for uncertainty estimates.

d. Ocean Heat Budget

208 The Gulf of Mexico is semi-enclosed basin and this provides a convenient opportunity to
209 study the heat budget. The heat budget of an oceanic water column may be calculated as
210 follows (Etter, 1983),

211 $$Q_t = Q_{net} + Q_v \qquad (3)$$

212 where Q_{net} is the net ocean surface heat flux and Q_v denotes the divergence of the heat
213 transport by ocean currents (advective heat flux). The bottom geothermal heat flux is small in
214 the GOM (Ochoa et al. 2021) and can be ignored in our analysis.

215 Q_{net} comprises net shortwave radiation flux (Q_{SWR}), net longwave radiation flux (Q_{LWR}),
216 surface latent heat flux (Q_{LAT}), and surface sensible heat flux (Q_{Sen}):

217 $$Q_{net} = Q_{SWR} + Q_{LWR} + Q_{LAT} + Q_{Sen} \qquad (4)$$

218 Q_{net} reflects the complex interaction between the ocean and the atmosphere (Carton et al.
219 2018). Knowing the annual net surface heat flux is important for understanding the heat
220 budget in the GOM. In this study, we analyze the Q_{net} from four representative products: a
221 fifth-generation atmospheric reanalysis of the global climate covering the period from
222 January 1979 to the present (ERA5; Hersbach et al. 2020) from the European Centre for
223 Medium-range Weather Forecasts, the Objectively Analyzed Air-Sea Fluxes (OAFlux; Yu et
224 al. 2008), NASA's Estimating the Circulation and Climate of the Ocean (ECCO version 4;
225 Forget et al. 2015) product, and the Simple Ocean Data Assimilation (SODA; Carton et al.
226 2018) improved reanalysis data.

227 Advective heat flux Q_v can be given by:

228 $$Q_v = \rho_w c_{pw} V \delta T \qquad (5)$$

229 where V is the Loop Current transport, which may be determined by the volume transport
230 across the Yucatán Channel (or Straits of Florida). δT is the average climatology temperature
231 difference between the Yucatán Channel and Straits of Florida. Bunge et al. (2002) and
232 Candela et al. (2019) showed that the volume transport across the Yucatán Channel V_Y and
233 the Florida Straits V_F should be balanced out ($V_Y \approx V_F \approx V$) on a multiple-year timescale
234 because river runoff and the volume transport due to precipitation minus evaporation are very
235 small in the GOM (~0.1% of V, Etter, 1983; Bunge et al. 2002) and the change of total
236 volume of water in the GOM with time is also a small term based on altimetry measurements
237 (Bunge et al. 2002).

3. Results

a. Warming Trend at Sea Surface

Fig. 3 shows the average surface temperature anomaly as a function of time for the GOM (red lines), the global ocean (black lines), and the subtropical northern Atlantic Ocean within the latitudinal band between 17.5˚N and 31.5˚N (blue lines). The region we selected in the Atlantic Ocean has the same latitudinal band as in the GOM for comparison purposes. There is a persistent warming trend in the Gulf of Mexico with a warming rate of ~0.193 ˚C decade^{-1} starting from around 1970 and the average temperature has increased by 1.0+ ˚C since 1970. The rate of warming in the Gulf of Mexico is about twice that for the global ocean (0.086 ˚C decade^{-1}), but only slightly larger than the warming trend in the subtropical northern Atlantic Ocean (0.183 ˚C decade^{-1}). This indicates that the subtropical northern Atlantic Ocean, including the GOM, likely has a larger warming rate than that for the global ocean and also shows the linkage between GOM and the tropical northern Atlantic Ocean. We also compared the GOM temperature anomaly at 0m with that at 10m and they are very similar (Fig. 3).

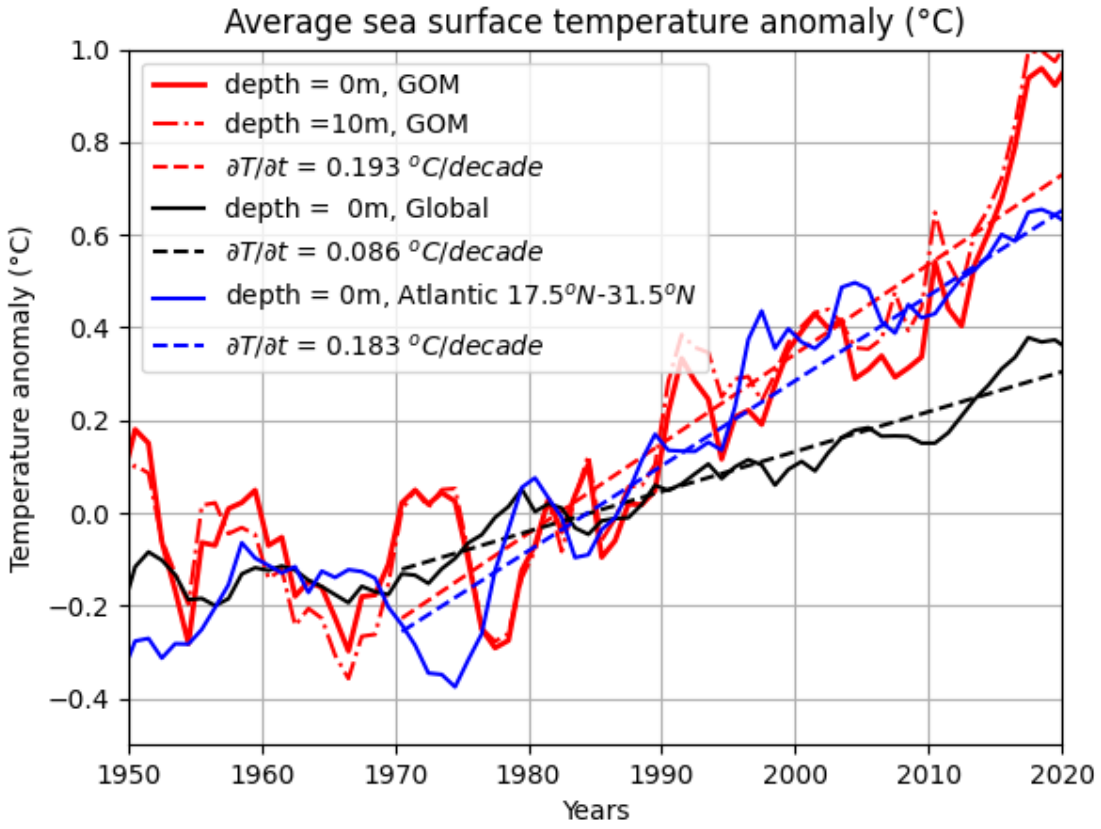

Fig. 3. Time series of the sea surface average temperature anomaly for the Gulf of Mexico (red), northern subtropical Atlantic Ocean between 17.5 and 31.5˚N latitudes (blue) and global oceans (black) based on running pentadal (five-year) analyses. The anomalies are related to a 1955-2006 (WOA09) baseline. Each pentadal estimate is plotted at the midpoint of the 5-year period. The dashed lines show the linear regression fitted lines for the period between 1970 and 2020 for the GOM, global and the subtropical northern Atlantic Ocean, respectively.

Our estimated warming rate of 0.193±0.05 ˚C decade^{-1} for the surface water of GOM is within the range of the rates (0.17~0.3 ˚C decade^{-1}) estimated by Muller-Karger et al. (2015) in the GOM based on satellite observed SST. Both our estimate and those by Muller-Karger et al. (2015) are slightly larger than the warming rate (0.15 ˚C decade^{-1}) for the Caribbean Sea estimated by Glenn et al. (2015) and the value (0.158 ˚C decade^{-1}) in Li et al. (2022). Levitus et al. (2012) showed the warming rates varied along latitudes for both global and basin-scale oceans. Within the same latitudinal band, the warming rate of the GOM and the northern Atlantic Ocean are similar (Fig. 3). Nonetheless, the surface warming rate in the GOM and surrounding oceans based on our estimates and estimates from previous studies are much larger (twice) than the warming rate of the global ocean (0.086 ˚C decade^{-1}). The faster warming rate at the sea surface may make the ecosystem and environment of GOM an area of higher susceptibility to climate change.

b. Subsurface Warming

Fig. 4a shows the temporal evolution and vertical distribution of the integrated OHC at each standard depth level for the GOM from 0 to 2000m. The y-axis is depths and the x-axis is time in years. The OHC is scaled by the thickness of each layer to make it comparable between layers as the thickness of the standard depths varies with depth. The same hatched areas as in Fig. 2 are plotted to show the poor data coverage periods. The vertical profile of the warming rates at each standard depth is shown in Fig. 4b. Simple linear regression is applied to compute the warming rate at each standard depth level and the gray area shows the variation of the warming rates with depth in Fig. 4b. The warming trend is most prominent near the surface in the upper 50m (Fig. 4a and 4b). The subsurface OHC change is more complicated. The warming rate rapidly declines with depth from 1.1×10^{17} J m^{-1} year^{-1} to 2.5×10^{16} J m^{-1} year^{-1} from 50m to 400m. The decline of warming rates decreases below 400m and becomes more uniform below 1100m. Between 200 and 600m, a subsurface irregular decadal warming and cooling oscillation (Fig. 4a) is found, which can also be seen from the

integrated 200-600m OHC shown in Fig. 4c. The entire vertical profile in Fig. 4b (black line) is positive indicating that oceanic warming occurs at all depths between surface and 2000m in the GOM. Ochoa et al. (2021) found that the deep-water below 2000m to the seafloor in the GOM was also warming in recent years. According to the warming trends in the upper 2000m shown in Fig. 4 and the warming shown in Ochoa et al. (2021) below 2000m, we can conclude that the overall trend of the entire GOM is warming in the past several decades from surface to bottom. Moreover, the Gulf of Mexico has warmed continuously since 1970 (Fig. 3 and Fig. 4) and the trend becomes steeper after 2010, at least at the surface (Fig. 3). The data coverage below 750m reduces substantially. There is much less spatial variability in the GOM temperature field below 750m than that is above. The seasonal cycle is also very small where it exists below 750 m and by 1000m, the entire GOM basin is approaching uniformity in temperature. A fewer number of spatially distributed measurements can represent the temperature anomaly of the basin below 750m.

The causes of the irregular subsurface decadal oscillation between 200 and 600m need more investigation. The period is approximately 10-30 years, much shorter than the Atlantic Multidecadal Oscillation (AMO), which has an estimated period of 60-80 years (McCarthy et al. 2015). Sediment core-derived annual SST indicated that AMO-like oscillations could occur in the Gulf of Mexico (Poore and Brock 2011), but our dataset is only 70 years long and we do not have enough evidence to link the decadal oscillation to AMO. The period is closer to that of the North Atlantic Oscillation (NAO), but NAO is largely an atmospheric phenomenon (Hurrell 1995). Our surface OHC does not show clear decadal oscillations as in the subsurface, and thus the subsurface oscillation is unlikely related to NAO. The interannual and decadal variability of the Loop Current transport flow through the Yucatán Channel may be one possible mechanism to explain the subsurface OHC oscillations between 200 and 600m, which needs long term observations (at least decades) of both current and temperature data at the Yucatán Channel to examine this, which currently is not available. Transport flow through the Yucatán Channel has only been measured in recent years but has already shown some interannual variations (Candela et al. 2019). More will be discussed in section 4a.

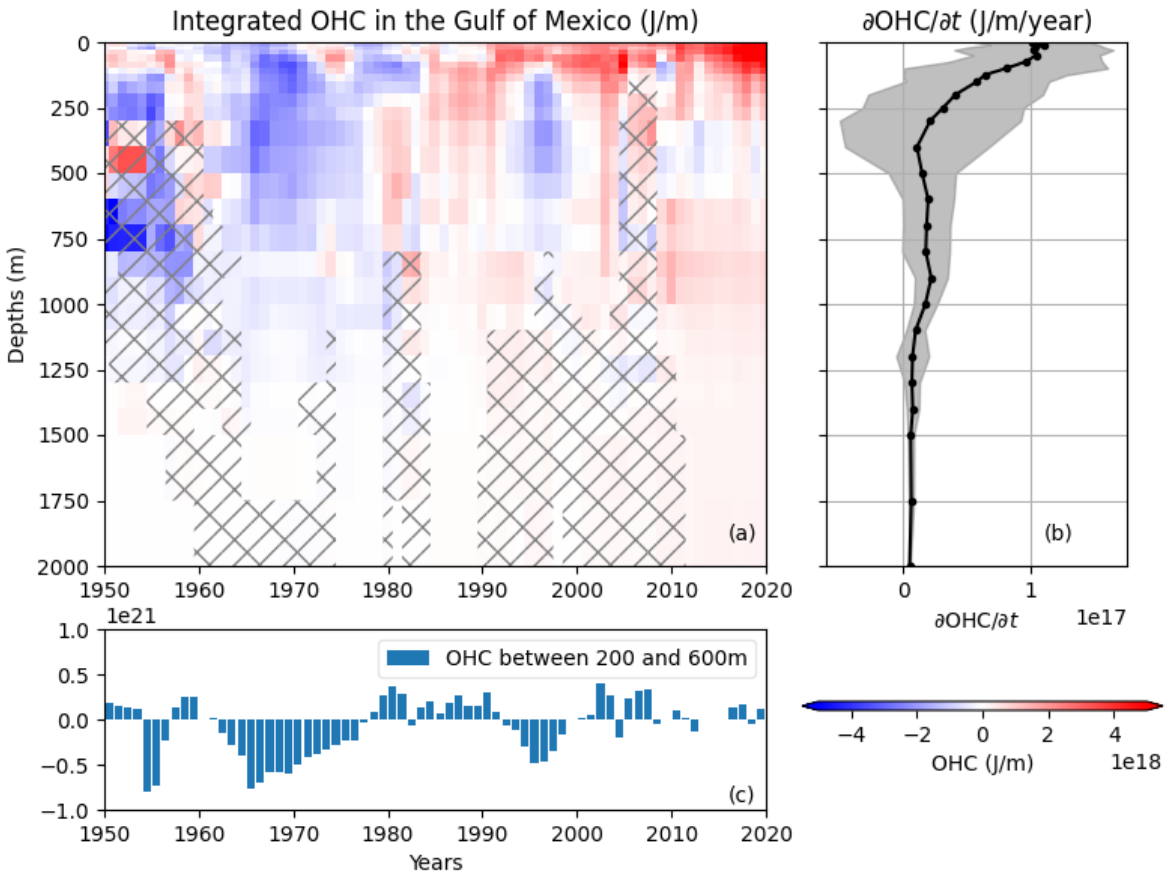

Fig. 4. (a) Spatially integrated OHC in the Gulf of Mexico between 1950 and 2020 as a function of depth (0-2000m) at standard depths. Hatched indicates the data coverage that is less than 30%. (b) The linear trend of OHC change in the GOM at standard depth levels. The rate is divided by the thickness of each layer to make them vertically comparable. The shading area shows the uncertainty of the linear trends (95% confidence intervals). The trend is estimated using linear regression for each standard depth between 1970 and 2020. The trends are statistically significant at all depths (p-value ≤ 0.05). Standard depths are defined as 0, 10, 20, 30, 50, 75, 100, 125, 150, 200, 250, 300, 400, 500, 600, 700, 800, 900, 1000, 1100, 1200, 1300, 1400, 1500, 1750, 2000m. Anomalies are relative to a 1955-2006 baseline. (c) Vertically integrated OHC between 200 and 600m.

c. Spatial Variations of the Warming Trends

To have a more detailed description of the spatial variations of the warming trends, we calculate the heat storage rate for each gridbox between selected depth ranges using linear regression between 1970 and 2020. In Fig. 5, we plot the color-coded heat storage rate at each gridbox for different selected depth layers. Besides the grids inside the GOM, we also show part of the Yucatán Basin of the Caribbean Sea in Fig. 5. Those grids in Yucatán Basin are not used in the trend estimates for the GOM in Figs. 3 and 4. Similar to what was shown in Fig. 4, the general trend in the upper 50 m (Fig. 5a) is warming, although the warming rate in the northeast Gulf is lower. The warming is largest in the mid-western GOM and at the

Yucatán channel in the upper 50m. Between 50 and 600 m (Fig. 5b and 5c), there is a slight cooling trend in the Northeast GOM. The rest of the GOM is warming with the Yucatán Channel having the largest warming rate over the entire GOM between 50 and 600m. Below 600m, warming occurs almost everywhere and the warming rate is smaller and more uniform. In summary, most of the Gulf of Mexico are warming in recent 50 years in the upper 2000m except for a small region in the northeastern GOM between 50 and 600m.

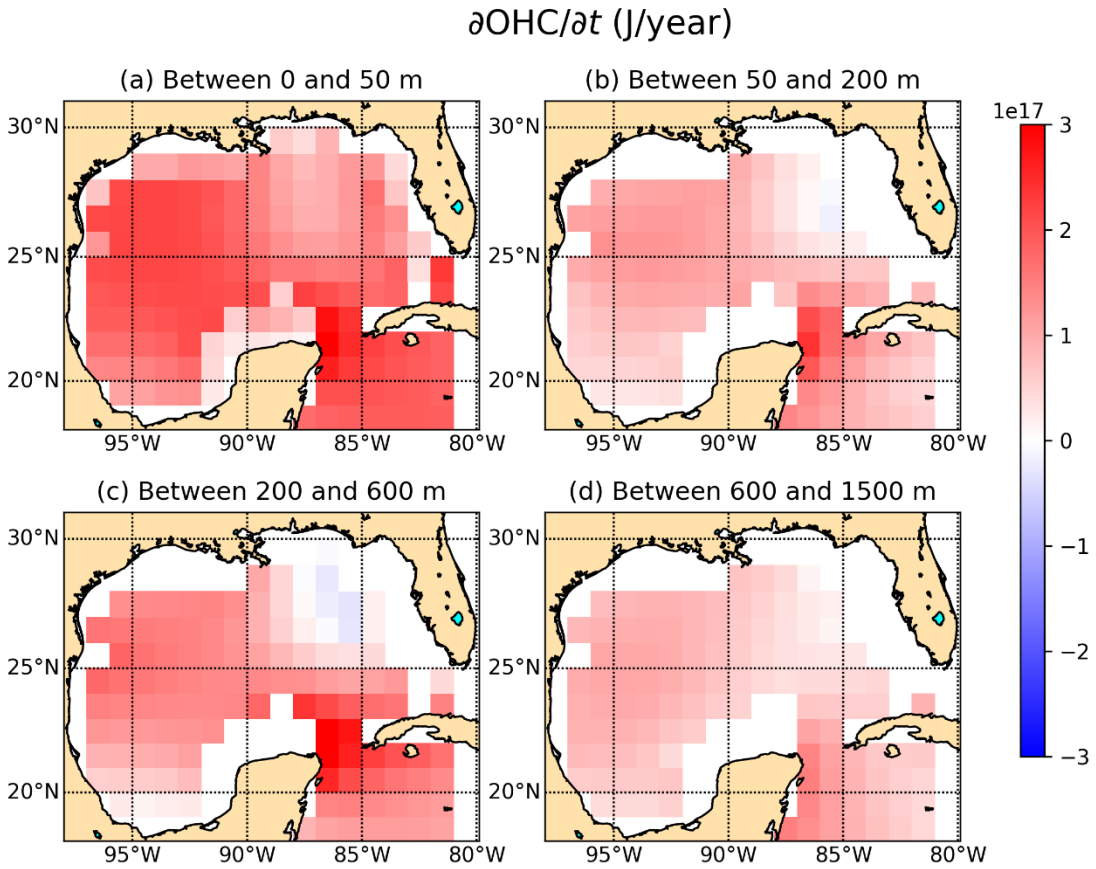

Fig. 5. Spatial distribution of the OHC change with time (units: J/year) between different layers (a) 0-50m; (b) 50-200m; (c) 200-600m; and (d) 600-1500m. The OHC trends are estimated using linear regression between 1970 and 2020 at each grid point between different depth layers.

4. Discussion

a. Ocean Heat Budget Closure

Based on Eq. (3), the rate of heat storage can be balanced with the annual net surface heat flux and the annual net advective heat flux, which are the two main forcings controlling the OHC change in the GOM. The GOM is a semi-enclosed basin with two narrow channels – Yucatán Channel and Straits of Florida – connecting with the surrounding oceans. The

354 geographical structure of the GOM makes it an ideal marginal sea to study the ocean heat
355 budget closure. We will quantify all three terms in Eq. (3) to examine the heat budget balance
356 in the GOM.

357 1) ESTIMATE OF HEAT STORAGE RATE Q_t

358 In Fig. 6, we plot the color-coded OHC between selected layers for the entire GOM in the
359 upper 2000m. The OHC becomes positive around 1980. About half of the warming after
360 1980 has occurred in the upper 200m and the upper 1000m accounts for 80-90% of the
361 warming in the upper 2000m. The heat storage rate of the upper 2000m in the GOM can be
362 estimated from the integrated OHC using linear regression. Although there are periods of
363 cooling (e.g. 1962-1971, 1992-2000) in the GOM, a warming trend is clear between 1970 and
364 2020 based on the integrated OHC in the upper 2000m (Fig. 6). Linear regression is applied
365 to the upper 2000m OHC between 1970 and 2020 (black line, Fig. 6) and between 1992 and
366 2017 (green line, Fig. 6), respectively, to estimate the ocean heat storage rates in the GOM.
367 The period of 1992 and 2017 is selected to have a common period with ECCO data for the
368 later heat budget closure discussion. The fit between 1970 and 2020 gives us an overall heat
369 storage rage in the past 50 years. The GOM OHC increases at 0.38±0.13 ZJ decade^{-1} (mean ±
370 uncertainty with 95% confidence interval) between 1970 and 2020 (r=0.76), which is
371 equivalent to 1.21±0.41 TW (1 TW = 10^{12} W). Ochoa et al. (2021) estimated the heat storage
372 rate below 2000m is approximately 0.17 TW (~0.054 ZJ decade^{-1}) in the GOM (uncertainty is
373 not given in Ochoa et al., 2021). Therefore, the total heat storage rate should be
374 approximately 1.38±0.41 TW for the entire water column of the GOM between 1970 and
375 2020. This is equivalent to 0.86±0.26 W m^{-2} if this is applied to the entire surface area of
376 GOM (1.60×10^{12} m^2). Correspondingly, the heat storage rate between 1992 and 2017 in the
377 GOM is approximately 0.50±0.43 ZJ decade^{-1} (Fig. 6, green line), which is equivalent to
378 1.59±1.36 TW. The full depth heat storage rate between 1992 and 2017 is about 1.76±1.36
379 TW considering the warming below 2000m from Ochoa et al. (2021) in the GOM or about
380 1.10±0.85 W m^{-2} applied to the entire surface area of GOM. The ocean heat storage rate
381 between 1992 and 2017 is larger than that for 1970~2020, primarily due to the cooling period
382 between 1992 and 2000.

383 The heat storage rates between 1970 and 2020 and between 1992 and 2017 (common
384 period of ECCO) in the GOM are both comparable to the full-depth ocean heat storage rate
385 for the global ocean estimated from observations between 1993 and 2020 by seven different

386 research groups, which is 0.82 to 1.11 W m^{-2} (Johnson et al., 2021) applied to the global
387 ocean surface (3.61×10^{14} m^2). See Table 3.2 in Johnson et al. (2021) for more details about
388 the trends of OHC increase for the global ocean. Note in Johnson et al. (2021), the ocean heat
389 storage rate is applied to Earth's entire surface. To compare ocean to ocean rate, we
390 converted the values in Johnson et al. (2021) to values for the global ocean surface. Although
391 SST (Figure 3) in the GOM suggest that the surface GOM is warming at a rate approximately
392 twice that of the global ocean, the full-depth ocean heat storage rate in the Gulf of Mexico is
393 similar to the rate for the global ocean.

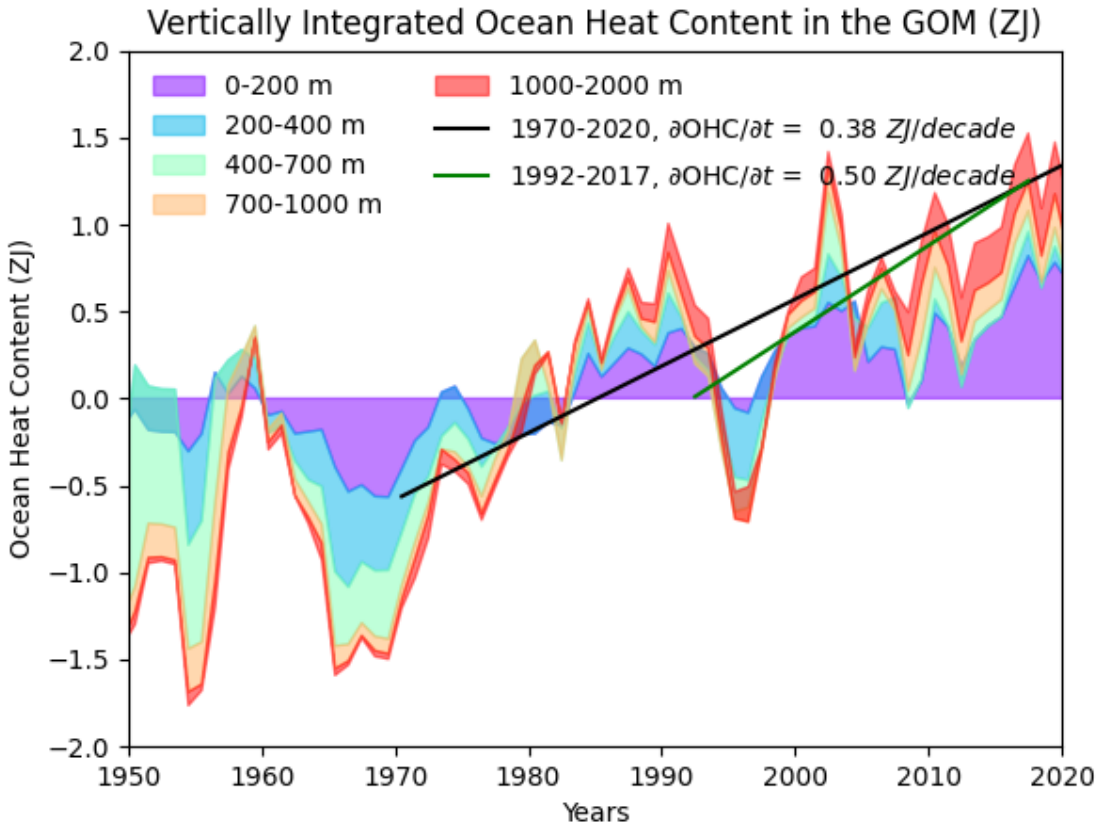

394

395 Fig. 6. Vertically integrated ocean heat content between selected layers of the entire
396 GOM from 1950 to 2020 between 0 and 2000m. The anomalies are related to a 1955-2006
397 (WOA09) baseline. The black line shows the linear regression fitted line based on the OHC
398 in the upper 2000m between 1970 and 2020. While the green line shows the fitted line
399 between 1992 and 2017 to have the same period as ECCO data.

400 2) NET ADVECTIVE HEAT FLUX

401 Based on Eq. (5), an accurate estimate of net advective heat flux requires long-term
402 simultaneous measurements of ocean current and temperature profiles at both the Yucatán
403 Channel and the Straits of Florida. Such observations are rare. The observations that have

been conducted are mostly short term (several months to several years) and focus on current observations across the Yucatán Channel to quantify the Loop Current transport through the GOM. One of the early efforts to measure the transport through the Yucatán Channel was conducted between 1999 and 2001 with an average transport estimated to be 23.8 Sv (1 Sv = 10^6 m^3s^{-1}) (Sheinbaum et al. 2002). Two latter efforts with more instruments were conducted between May 2010 and May 2011 and between July 2012 and June 2013 with estimated transport to be 27.1 Sv and 25.0 Sv, respectively (Athié et al. 2015). The variability in transport at Yucatán Channel was found to be well correlated with a transport proxy based on altimetry data (Athié et al. 2015). The most recent observations were carried out between September 2012 and August 2016 by Candela et al. (2019) across both Yucatán Channel and Straits of Florida. The average transport at both channels was 27.6 Sv based on the four years of continuous observations. The transports though the western ends of Straits of Florida were estimated to be ~25 Sv for an 11-month period between December 1990 and November 1991 (Hamilton et al. 2005), which also agreed well with transport across Yucatán Channel. A long-term monitoring program measured daily flow between Florida and the Bahamas at the Cable section (~26.7°N), which can be considered as a surrogate for the Loop Current flow. The Cable estimated annual mean flow is approximately 31~32 Sv (Schmitz and McCartney 1993; Larsen & Sanford 1985; Volkov et al. 2020), which should be slightly larger than the actual Loop Current flow at the Yucatán Channel or Straits of Florida due to the inputs from the Old Bahama and the Northwest Providence Channels (Hamilton et al. 2005; Candela et al. 2019). From these limited observations, the transport flow through the GOM via the two channels may range from 23.8 to less than 32 Sv. We will use V = 27.6±4.0 Sv as the Loop Current transport flow in our following calculation by considering the value in Candela et al. (2019) is based on the longest (4 years) observations at both Yucatán Channel and Florida Straits and also considering the large variations from other studies. We assume the transport through Yucatán Channel and Straits of Florida are the same (Bunge et al. 2002).

In order to calculate the advective heat flux Q_v, we also need to know the average climatology temperature difference between the Yucatán Channel and the Straits of Florida (Fig. 7). We use the 0.1°×0.1° GOM Regional Climatology V2 temperature fields in our analysis, which is also derived from the WOD18 using the same temperature profiles used in the above warming trend estimation. The average vertical temperature profiles at the two channels are similar with the maximum difference found between 50 and 300 m (Fig. 7). The vertical mean temperature difference δT in the upper 1000m is approximately 0.36±0.02 °C

(Fig. 7b). The temperature difference is calculated only in the upper 1000m because the sill depth at the Florida Straits is only about 1000m (730m at its shallowest point). There might be small compensation deep flows into the Caribbean Sea below 1000m at the Yucatán Channel (Maul et al. 1985; Bunge et al. 2002). Candela et al. 2019 showed that deep circulation contributes minimally to the overall transport of the Loop Current and therefore is not considered in this simplified calculation. Abascal et al. (2003) showed the water temperature at a given depth was cooler at the Yucatan coast and the transport was more concentrated near the Yucatan coast. We did not consider variations in the advective heat flux calculation due to the across-strait structure of the temperature section at two channels when calculating the mean temperature profile difference, which might introduce some errors/uncertainties. Substituting $V = 27.6 \pm 4.0$ Sv and $\delta T = 0.36 \pm 0.02$ °C into Eq. (5), we estimate the advective net heat flux Q_v to be 40.7±6.3 TW. Climate models estimated Loop Current advective heat flux through the GOM in the late 20th century to be 54.9 TW using high-resolution model or 24.9 TW if low-resolution model is used (Liu et al. 2012). Our estimate lies between the two model estimates.

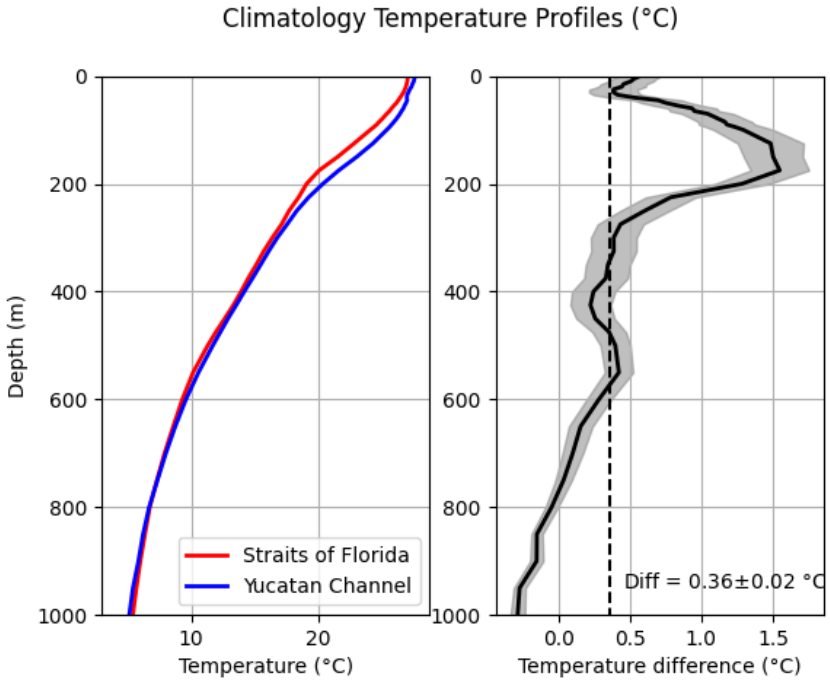

Fig. 7 (a) Climatology mean temperature profiles at Straits of Florida and Yucatán Channel in the upper 1000m. (b) The temperature difference between the Yucatán Channel and the Straits of Florida. The shaded area shows ±1 standard deviation (std). The dashed vertical is the vertical mean of the temperature difference. 0.1°×0.1° regional climatological temperature fields for the GOM (https://www.ncei.noaa.gov/products/gulf-mexico-regional-climatology) are used. The profile for Straits of Florida is averaged from all profiles within an

area with latitudes between 23° and 25°N and longitudes between -81.1° and -80.2°. The profile for Yucatán Channel is averaged from all profiles within an area with latitudes of 21°-21.9°N and longitudes of -86.8° to -84.9°.

Liu et al. (2012) discussed that the advection flow (Loop Current) into the GOM may slow down (20-25% reduction) in the late 21st century based on climate model predictions. The consequence of a weakening Loop Current is less advective heat flux into the GOM and a cooling impact in the GOM, particularly in the northern basin based on the high-resolution Miami Isopycnic Coordinate Ocean Model (Liu et al. 2012). The transport flow observations at the Yucatán Channel (Sheinbaum et al. 2002; Athié et al. 2015; Candela et al. 2019) and the Florida Cable observations (Larsen and Sanford 1985; Volkov et al. 2020) did not show obvious evidence of the slowing down of the advective heat flux into the GOM. However, the northeastern GOM is indeed less affected by the warming between 1970 and 2020 (Fig. 5), which is coincidentally consistent with the prediction in Liu et al. (2012). The advective net heat flux may be affected by eddies and wind in the GOM and cause inter-annual variabilities. Using a numerical model, Chang and Oey (2010) found that a steady, uniform westward wind in the GOM could increase the heat input into the GOM via the Yucatán Channel as the wind-induced shelf currents advect more heat westward to the western Gulf. They also found eddies were effective transporters of heat across the central Gulf. Seasonality, interannual variability, and intraseasonal variability of wind fields and frequency of Loop Current eddy shedding (Zavala-Hidalgo et al. 2014) could all cause variations in the advective heat flux through the GOM, which contribute to variations of OHC in the upper ocean shown in Figures 4 and 6.

3) Net Surface Heat Flux

We compare net surface heat flux in the GOM from four different products as listed in Section 2d. All products show that the northern and eastern GOM lose heat to the atmosphere, while the southwestern GOM gains heat from the atmosphere on an annual basis (Fig. 8). It should be noted that the ECCO data show a larger heat loss area (Fig. 8d) than the other three products. The net surface heat flux averaged over the entire GOM is positive for SODA and OAFlux, but negative for ERA5 and ECCO (Fig. 8 and Table 2). The annual cycles of the net surface heat fluxes in the GOM (Fig. 9) are similar in magnitude for all products. The GOM loses heat to the atmosphere in Fall, Winter and early Spring and gains heat in late Spring and Summer. Except for ECCO, their annual mean values are centered

around zero. The ECCO annual values are offset towards negative values (losing heat to the atmosphere). The long-term average values of SODA and OAFlux suggest the GOM gains heat from the atmosphere at a rate of 3.9 $W\,m^{-2}$ and 6.7 $W\,m^{-2}$, respectively; while the ERA5 loses heat to the atmosphere at a rate of -3.9 $W\,m^{-2}$ annually. ECCO data shows that the GOM loses a large amount of heat to the atmosphere every year at a rate of -23.7 $W\,m^{-2}$. Whether GOM gains heat from the atmosphere or loses heat to the atmosphere on an annual basis is still an open question. Previous estimates of the annual average net surface heat flux in the GOM varied from -34.1 $W\,m^{-2}$ to 46.6 $W\,m^{-2}$ (Table 2) or -54.6 to 74.6 TW for the entire surface area of the GOM (area = 1.60 $\times 10^{12}$ m^2). Large differences might be due to the different methodologies, coefficients, formulas, and datasets used in these studies (Zavala-Hidalgo et al. 2002; Zavala-Hidalgo et al. 2014; Liang et al. 2016). A heat budget analysis will help us to determine the sign of the net annual surface heat flux over the entire GOM.

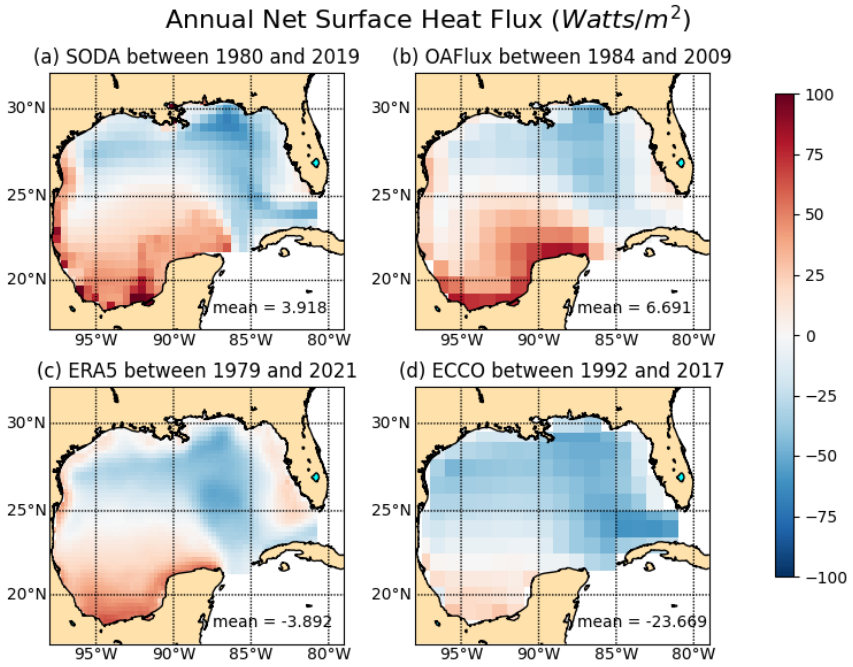

Fig. 8. Spatial distribution of the annual net surface heat flux (units: $W\,m^{-2}$) from (a) SODA, (b) OAFlux, (c) ERA5 and (d) ECCO. Note the average period is based on the available years of each dataset and shown on the top of each panel.

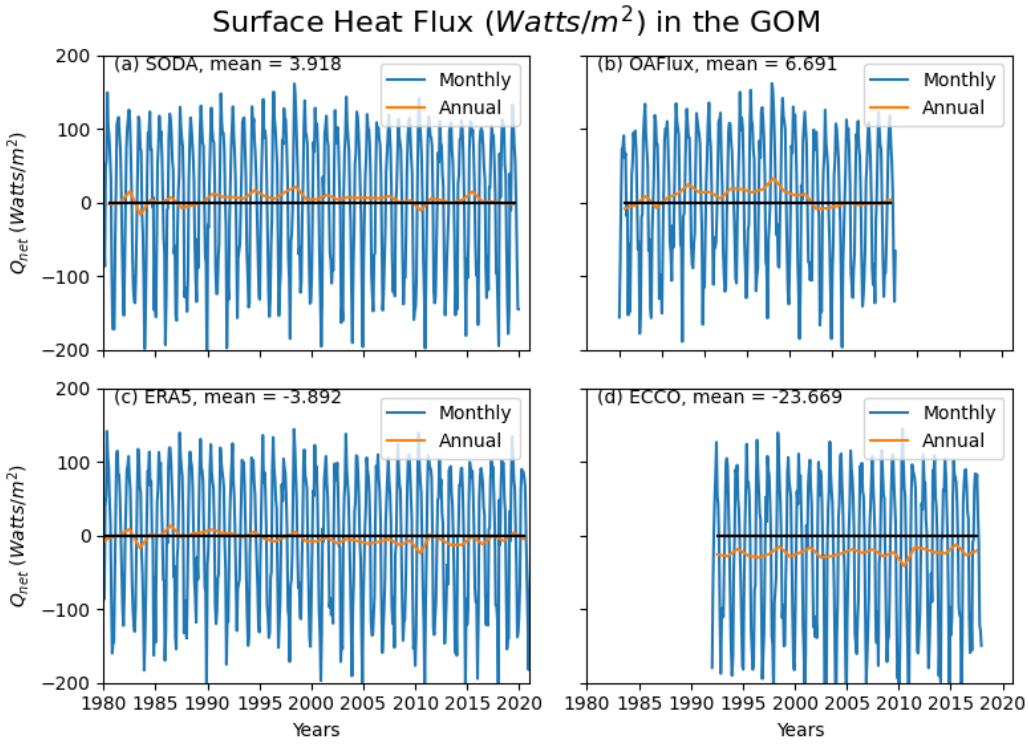

508

509 Fig. 9. Time series of monthly and annual surface heat flux for (a) SODA, (b) OAFlux,
510 (c) ERA5, and (d) ECCO. Blue: monthly surface heat flux for the GOM; red: annual surface
511 heat flux for the GOM. The long-term mean over the available data period for each product is
512 shown at the top of each panel.

513

Sources	Annual surface net heat flux ($W\ m^{-2}$)	Annual surface net heat flux (TW) of the entire GOM using the surface area of GOM = 1.60×10^{12} m^2
Hasternrath (1986)	-15.1	-24.2
Etter (1983)	-24.0	-38.4
Adem et al. (1993)	-2.2	-3.5
Zavala-Hidalgo et al. (2002), bulk formulas	46.6	74.6
Zavala-Hidalgo et al. (2002), satellites and empirical formulas	9.0	14.4
Liu et al. (2012), climate model, high resolution	-34.1	-54.6
Liu et al. (2012), climate model, low resolution	-18.9	-24.4
ERA5 (this study)	-3.9	-6.2
SODA (this study)	3.9	6.2

OAFlux (this study)	6.7	10.7
ECCO (this study)	-23.7	-37.9
Heat budget estimate (this study)	-24.3±4.1	-38.9±6.5

Table 2. Annual net surface heat flux from previous studies and from four global products (ERA5, SODA, OAFlux and ECCO).

4) HEAT BUDGET CLOSURE

The heat storage rate in the GOM 1.76±1.36 TW between 1992 and 2017 (the same period of ECCO) based on the calculation from the OHC change in the upper 2000m and the estimate below 2000m in Ochoa et al. (2021), while the advective net heat flux is estimated to be 40.7±6.3 TW, which is more than 20 times larger than the heat storage rate. Based on Eq. (3), the GOM needs to release heat to the atmosphere at a rate approximately of -38.9±6.5 TW; otherwise, the GOM would warm at a faster rate. Etter (1983)'s estimate of -38.4 TW and the value from ECCO -37.9 TW are comparable to the estimate from Eq. (3) by taking the difference between advective net heat flux and heat storage rate between 1992 and 2017 (Table 2). Due to the fact that the average annual temperature difference between the Yucatán Channel and the Straits of Florida are almost always positive and the heat storage rate is much smaller than the advective heat flux, we would expect that the annual net surface heat flux should be negative. Based on the ocean heat closure in Eq. (3), the annual net surface heat flux from ECCO is the closest one among the four products to close the heat budget in the GOM. Note that the ECCO net surface heat flux is based on a non-linear inverse modeling framework that satisfies both ocean dynamics and data constraints (Forget et al. 2015). Wunsch (2011) also stated that the "adjoint method" used in ECCO made the resulting state estimate satisfies known equations of motion and conservation laws. That might be the reason why ECCO provides the closest net surface heat flux to close the heat budget in the GOM.

b. Impact of Warming in the GOM

The persistent warming in the GOM (Figs. 3-6) could have already influenced the marine ecosystem and organisms in the Gulf of Mexico. Jordán-Dahlgren et al. (2005) found that surface water warming might increase the prevalence of coral diseases in the northeast Caribbean and Gulf of Mexico by enhancing pathogen activity. Warming also had negative effects on survivorship of the deep-sea coral *Lophelia pertusa* in the Gulf of Mexico based on a series of warming treatment experiments (Lunden et al. 2014). Atlantic Bluefin tuna (BFT)

543 spawns predominantly in the northern GOM with the optimal spawning temperature of 24-27
544 ˚C from April to June (Schaefer, 2001). The increased upper ocean temperature (Figs. 3 and
545 4) could reduce the areas in the northern GOM with BFT optimal spawning conditions
546 (Muhling et al. 2011). Warming produces a poleward shift in the distribution of many
547 organisms. For example, numerous additions to the fish fauna were discovered by comparing
548 fish assemblages within seagrass meadows of the northern GOM between the 1970s and
549 2006-2007 survey data (Fodrie et al. 2010). GOM has one of the world's largest
550 eutrophication-driven coastal hypoxia zones and warming will only exacerbate hypoxic
551 conditions (Boesch 2008; Laurent et al. 2018).

552 GOM is one of the marginal seas with frequent hurricane formations and landfalls each
553 year. Hurricane intensity is sensitive to changes in SST (Emanuel 2005) and OHC in the
554 upper ocean (Hallam et al. 2021; Eley et al. 2021). A 0.5 ˚C increase in August-September
555 SST is responsible for a 40% increase in hurricane activity and frequency (Saunders and Lea
556 2008) based on a statistical model. Hurricane prediction model results show the frequency of
557 category 4 and 5 storms could be doubled by the end of the 21st century due to global
558 warming, and the largest increase is projected to occur in the Western Atlantic Ocean and
559 Gulf of Mexico (Bender et al. 2010). The average SST has increased by approximately 1.0 ˚C
560 (Fig. 3) and the OHC increase is most prominent in the upper 200m (Fig. 4) since the 1970s,
561 which contribute to the recent intensified hurricane activities in the Gulf of Mexico e.g.
562 Hurricane Harvey (Trenberth et al. 2018) and Hurricane Michael (Nyadjro et al. 2021).
563 Hurricane rainfall dependency increases by a factor of five when SSTs range from 26 to 29
564 ˚C (Folkins and Braun 2003).

565 Although the Gulf of Mexico is a semi-enclosed marginal sea, its warming is sensitive to
566 climate change in the Caribbean Sea and North Tropical Atlantic Ocean (Ochoa et al. 2021;
567 Chollett et al. 2012). Long-term monitoring of the heat transport through the Yucatán
568 Channel is necessary to understand the controlling mechanisms of the warming in the GOM.
569 The role of the Loop Current and Loop Current eddies in controlling the warming also needs
570 more investigation.

571 5. Summary

572 OHC in the Gulf of Mexico is calculated from the World Ocean Database 2018 (Boyer et
573 al. 2018) with 1˚×1˚ spatial resolution for the upper 2000m and is available from 1950 to

2020. The warming/cooling trends are quantified based on the change of OHC at both basin and grid scales using a linear regression method. We have estimated a warming rate of 0.38±0.13 ZJ/decade (0.76±0.26 W m^{-2}) over the upper 2000m in the GOM in 50 years between 1970 and 2020. The warming rate for the entire GOM between 1970 and 2020 is 0.86±0.26 W m^{-2} (0.76 W m^{-2} in the upper 2000m + 0.1 W m^{-2} below 2000m (Ochoa et al. 2021)), which is comparable to the warming rate of the global ocean (0.82-1.11 W m^{-2}, Johnson et al., 2021). Warming occurs at all depths from the sea surface to bottom with the largest warming rates found in the upper 50m (Fig. 4b and Ochoa et al. 2021). The rate of the warming trend at the surface is about twice that for the global ocean (Fig. 3). A subsurface decadal warming and cooling oscillation with irregular periods is found between 200 and 600 m. Most regions of the GOM show a warming trend between 1970 and 2020, except for a subsurface region in the northeastern GOM. Based on the ocean heat budget, the GOM should lose heat to the atmosphere and the annual net negative surface heat flux from the ECCO can roughly close the heat budget in the GOM. The Loop Current advective heat flux is the main heat source for the warming in the GOM. The southern GOM gains heat from the atmosphere on the annual time scale, but integrated over the entire basin, the GOM loses heat to the atmosphere.

Understanding the spatial and temporal evolution of the warming trend in the Gulf of Mexico is critical to advance the understanding of environmental change since the 1970s. The warming in the Gulf of Mexico could cause a series of environmental issues, for example, sea level rise and the incidence of hypoxia. Warming also increases the intensity of hurricanes, which leads to the potential loss of wetlands and damage to coastal communities. Warming could cause increased stratification and reduce the O_2 solubility of the water. Less nutrients can be mixed into the surface waters due to enhanced stratification, which will have a negative impact on phytoplankton production and eventually on marine species and commercial fisheries. Here we have shown that most regions of the GOM have become warmer since the 1970s. We hope this study may inspire more investigations on the relationship between warming and environmental issues in the GOM.

Acknowledgments.

This work was supported by the NOAA National Centers for Environmental Information (NCEI) and NOAA grant 363541-191001-021000 (Northern Gulf Institute) at Mississippi State University. The authors would like to thank the scientists and data providers for

606 continuing to share their data, data managers and our NCEI colleagues for stewarding the
607 data for long-term preservation, and the NCEI Ocean Climate Laboratory colleagues for
608 continuing to enhance and maintain the World Ocean Database. Without this combined
609 effort, data-based studies like this would not be possible. We thank S. Cross, D. Dukhovskoy,
610 H.M. Zhang, J. Carton and other NCEI colleagues for valuable conversations.

611 *Data Availability Statement.*

612 We used the most recent version of the World Ocean Database published online in 2018
613 (WOD18) and available at https://www.ncei.noaa.gov/products/world-ocean-database. GOM
614 Regional Climatology data is available at https://www.ncei.noaa.gov/products/gulf-mexico-
615 regional-climatology. ERA5 surface heat flux is available at
616 https://www.ecmwf.int/en/forecasts/datasets/reanalysis-datasets/era5; OAFlux is available at
617 https://oaflux.whoi.edu/data-access/; ECCO surface heat flux is available at
618 https://cmr.earthdata.nasa.gov/virtual-directory/collections/C1990404812-
619 POCLOUD/temporal; and SODA data is available at
620 https://www2.atmos.umd.edu/~ocean/index_files/soda3.4.2_mn_download_b.htm.

621

622

623 REFERENCES

624 Abascal, A. J., Sheinbaum, J., Candela, J., Ochoa, J., & Badan, A. (2003). Analysis of flow
625 variability in the Yucatan Channel. *Journal of Geophysical Research: Oceans*, 108(C12).

626 Adem, J., Villanueva, E. E., & Mendoza, V. M. (1993). A new method for estimating the
627 seasonal cycle of the heat balance at the ocean surface, with application to the Gulf of
628 Mexico. *Geofísica Internacional*, *32*(1), 21-34.

629 Alory, G., & Meyers, G. (2009). Warming of the upper equatorial Indian Ocean and changes
630 in the heat budget (1960–99). *Journal of Climate*, *22*(1), 93-113.

631 Athié, G., Sheinbaum, J., Leben, R., Ochoa, J., Shannon, M. R., & Candela, J. (2015).
632 Interannual variability in the Yucatan Channel flow. *Geophysical Research Letters*, *42*(5),
633 1496-1503.

634 Bender, M. A., Knutson, T. R., Tuleya, R. E., Sirutis, J. J., Vecchi, G. A., Garner, S. T., &
635 Held, I. M. (2010). Modeled impact of anthropogenic warming on the frequency of
636 intense Atlantic hurricanes. *Science*, *327*(5964), 454-458.

637 Boesch, D. F. (2008). Global warming and coastal dead zones. *Disponible en línea en:*
638 *http://www. umces. edu/sites/default/files/pdfs/db_WarmingDeadZones. pdf (consultado*
639 *el 25 de agosto, 2013)*.

640 Boyer, T. P., Baranova, O. K., Coleman, C., Garcia, H. E., Grodsky, A., Locarnini, R. A.,
641 Mishonov, A. V., Paver, C. R., Reagan, J. R., Seidov, D., I., Smolyar, V., Weathers, K.,
642 Zweng, M. M. (2018). World Ocean Database 2018. A. V. Mishonov, Technical Editor,
643 *NOAA Atlas NESDIS* 87.

644 Bunge, L., Ochoa, J., Badan, A., Candela, J., & Sheinbaum, J. (2002). Deep flows in the
645 Yucatan Channel and their relation to changes in the Loop Current extension. *Journal of*
646 *Geophysical Research: Oceans*, *107*(C12), 26-1.

647 Candela, J., Ochoa, J., Sheinbaum, J., Lopez, M., Perez-Brunius, P., Tenreiro, M., ... &
648 Arriaza-Oliveros, L. (2019). The flow through the gulf of Mexico. *Journal of Physical*
649 *Oceanography*, *49*(6), 1381-1401.

650 Carton, J. A., Chepurin, G. A., Chen, L., & Grodsky, S. A. (2018). Improved global net
651 surface heat flux. *Journal of Geophysical Research: Oceans*, *123*(5), 3144-3163.

652 Chollett, I., Müller-Karger, F. E., Heron, S. F., Skirving, W., & Mumby, P. J. (2012).
653 Seasonal and spatial heterogeneity of recent sea surface temperature trends in the
654 Caribbean Sea and southeast Gulf of Mexico. *Marine pollution bulletin*, *64*(5), 956-965.

655 Cohen, D. (2018). Coastline County Population Continues to Grow. *The United States*
656 *Census Bureau. https://www. census. gov/library/stories/2018/08/coastal-county-*
657 *populationrises. html (November 30, 2019)*.

658 Eley, E. N., Subrahmanyam, B., & Trott, C. B. (2021). Ocean–Atmosphere Interactions
659 during Hurricanes Marco and Laura (2020). *Remote Sensing*, *13*(10), 1932.

660 Emanuel, K. (2005). *Divine wind: the history and science of hurricanes*. Oxford university
661 press.

662 Etter, P. C. (1983). Heat and freshwater budgets of the Gulf of Mexico. *Journal of physical*
663 *oceanography*, *13*(11), 2058-2069.

664 Fodrie, F. J., Heck Jr, K. L., Powers, S. P., Graham, W. M., & Robinson, K. L. (2010).
665 Climate-related, decadal-scale assemblage changes of seagrass-associated fishes in the
666 northern Gulf of Mexico. *Global Change Biology*, *16*(1), 48-59.

667 Folkins, I., & Braun, C. (2003). Tropical rainfall and boundary layer moist entropy. *Journal*
668 *of climate*, *16*(11), 1807-1820.

669 Forget, G. A. E. L., Campin, J. M., Heimbach, P., Hill, C. N., Ponte, R. M., & Wunsch, C.
670 (2015). ECCO version 4: An integrated framework for non-linear inverse modeling and
671 global ocean state estimation. *Geoscientific Model Development*, *8*(10), 3071-3104.

672 Glenn, E., Comarazamy, D., González, J. E., & Smith, T. (2015). Detection of recent regional
673 sea surface temperature warming in the Caribbean and surrounding region. *Geophysical*
674 *Research Letters*, *42*(16), 6785-6792.

675 Hallam, S., Guishard, M., Josey, S. A., Hyder, P., & Hirschi, J. (2021). Increasing tropical
676 cyclone intensity and potential intensity in the subtropical Atlantic around Bermuda from
677 an ocean heat content perspective 1955–2019. *Environmental Research Letters*, *16*(3),
678 034052.

679 Hamilton, P., Larsen, J. C., Leaman, K. D., Lee, T. N., & Waddell, E. (2005). Transports
680 through the Straits of Florida. *Journal of physical oceanography*, *35*(3), 308-322.

681 Hastenrath, S. L. (1968). ESTIMATES OF THE LATENT AND SENSIBLE HEAT FLUX
682 FOR THE CARIBBEAN SEA AND THE GULF OF MEXICO 1. *Limnology and*
683 *Oceanography*, *13*(2), 322-331.

684 Hersbach, H., Bell, B., Berrisford, P., Hirahara, S., Horányi, A., Muñoz-Sabater, J., ... &
685 Thépaut, J. N. (2020). The ERA5 global reanalysis. *Quarterly Journal of the Royal*
686 *Meteorological Society*, *146*(730), 1999-2049.

687 Hurrell, J. W. (1995). Decadal trends in the North Atlantic Oscillation: Regional temperatures
688 and precipitation. *Science*, *269*(5224), 676-679.

689 IPCC (2021). Climate Change 2021: The Physical Science Basis. Contribution of Working
690 Group I to the Sixth Assessment Report of the Intergovernmental Panel on Climate
691 Change [Masson-Delmotte, V., P. Zhai, A. Pirani, S.L. Connors, C. Péan, S. Berger, N.
692 Caud, Y. Chen, L. Goldfarb, M.I. Gomis, M. Huang, K. Leitzell, E. Lonnoy, J.B.R.
693 Matthews, T.K. Maycock, T. Waterfield, O. Yelekçi, R. Yu, and B. Zhou (eds.)].
694 Cambridge University Press. In Press.

695 Johnson, G. C., Lyman, J. M., Boyer, T., Cheng, L., Gilson, J., Ishii, M., Killick, R. E. &
696 Purkey, S. G. (2021) Ocean heat content [in "State of the Climate in 2020"]. Bull. Amer.
697 Meteor. Soc., 102 (8), S164–S169, https://doi.org/10.1175/ BAMS-D-21-0083.1.

698 Jordán-Dahlgren, E., Maldonado, M. A., & Rodríguez-Martínez, R. E. (2005). Diseases and
699 partial mortality in Montastraea annularis species complex in reefs with differing
700 environmental conditions (NW Caribbean and Gulf of México). *Diseases of aquatic*
701 *organisms*, *63*(1), 3-12.

702 Kuffner, I. B., Lidz, B. H., Hudson, J. H., & Anderson, J. S. (2015). A century of ocean
703 warming on Florida Keys coral reefs: historic in situ observations. *Estuaries and*
704 *Coasts*, *38*(3), 1085-1096.

705 Larsen, J. C., & Sanford, T. B. (1985). Florida Current volume transports from voltage
706 measurements. *Science*, *227*(4684), 302-304.

707 Laurent, A., Fennel, K., Ko, D. S., & Lehrter, J. (2018). Climate change projected to
708 exacerbate impacts of coastal eutrophication in the northern Gulf of Mexico. *Journal of*
709 *Geophysical Research: Oceans*, *123*(5), 3408-3426.

Levitus, S., Antonov, J. I., Boyer, T. P., Locarnini, R. A., Garcia, H. E., & Mishonov, A. V. (2009). Global ocean heat content 1955–2008 in light of recently revealed instrumentation problems. *Geophysical Research Letters*, 36(7).

Levitus, S., Antonov, J. I., Boyer, T. P., Baranova, O. K., Garcia, H. E., Locarnini, R. A., ... & Zweng, M. M. (2012). World ocean heat content and thermosteric sea level change (0–2000 m), 1955–2010. *Geophysical Research Letters*, *39*(10).

Lee, C.M., Rudnick, D.L. (2018). Underwater Gliders. In: Venkatesan, R., Tandon, A., D'Asaro, E., Atmanand, M. (eds) Observing the Oceans in Real Time. Springer Oceanography. Springer, Cham. https://doi.org/10.1007/978-3-319-66493-4_7

Li, G., Wang, Z., & Wang, B. (2022). Multidecade Trends of Sea Surface Temperature, Chlorophyll-a Concentration, and Ocean Eddies in the Gulf of Mexico. *Remote Sensing*, 14(15), 3754.

Liang, X., & Yu, L. (2016). Variations of the global net air–sea heat flux during the "hiatus" period (2001–10). *Journal of Climate*, *29*(10), 3647-3660.

Liu, Y., Lee, S. K., Muhling, B. A., Lamkin, J. T., & Enfield, D. B. (2012). Significant reduction of the Loop Current in the 21st century and its impact on the Gulf of Mexico. *Journal of Geophysical Research: Oceans*, *117*(C5).

Locarnini, R. A., Mishonov, A. V., Baranova, O. K., Boyer, T. P., Zweng, M. M., Garcia, H. E., Reagan, J. R., Seidov, D., Weathers, K., Paver, C. R., and Smolyar, I. (2018). World Ocean Atlas 2018, Volume 1: Temperature. A. Mishonov Technical Ed.; *NOAA Atlas NESDIS* 81, 52 pp.

Lunden, J. J., McNicholl, C. G., Sears, C. R., Morrison, C. L., & Cordes, E. E. (2014). Acute survivorship of the deep-sea coral Lophelia pertusa from the Gulf of Mexico under acidification, warming, and deoxygenation. *Frontiers in Marine Science*, 1, 78.

Maul, G. A., Mayer, D. A., & Baig, S. R. (1985). Comparisons between a continuous 3-year current-meter observation at the sill of the Yucatan Strait, satellite measurements of Gulf Loop Current area, and regional sea level. *Journal of Geophysical Research: Oceans*, *90*(C5), 9089-9096.

738 McCarthy, G. D., Haigh, I. D., Hirschi, J. J. M., Grist, J. P., & Smeed, D. A. (2015). Ocean
739 impact on decadal Atlantic climate variability revealed by sea-level
740 observations. *Nature*, *521*(7553), 508-510.

741 McKinney, L. D., Shepherd, J. G., Wilson, C. A., Hogarth, W. T., Chanton, J., Murawski, S.
742 A., ... & Caffey, R. (2021). The Gulf of Mexico. *Oceanography*, *34*(1), 30-43.

743 Muhling, B. A., Lee, S. K., Lamkin, J. T., & Liu, Y. (2011). Predicting the effects of climate
744 change on bluefin tuna (Thunnus thynnus) spawning habitat in the Gulf of Mexico. *ICES*
745 *Journal of Marine Science*, *68*(6), 1051-1062.

746 Muller-Karger, F. E., Smith, J. P., Werner, S., Chen, R., Roffer, M., Liu, Y., ... & Enfield, D.
747 B. (2015). Natural variability of surface oceanographic conditions in the offshore Gulf of
748 Mexico. *Progress in Oceanography*, *134*, 54-76.

749 Nyadjro, E. S., Wang, Z., Reagan, J., Cebrian, J., & Shriver, J. F. (2021). Bio-Physical
750 Changes in the Gulf of Mexico During the 2018 Hurricane Michael. *IEEE Geoscience*
751 *and Remote Sensing Letters*.

752 Ochoa, J., Ferreira-Bartrina, V., Candela, J., Sheinbaum, J., López, M., Pérez-Brunius, P., ...
753 & Amon, R. M. (2021). Deep-Water Warming in the Gulf of Mexico from 2003 to
754 2019. *Journal of Physical Oceanography*, *51*(4), 1021-1035.

755 Panofsky, H.A. and Brier, G.W., 1958. Some applications of statistics to meteorology.
756 Mineral Industries Extension Services, College of Mineral Industries, Pennsylvania State
757 University.

758 Poore, R. Z., & Brock, J. C. (2011). *Evidence of multidecadal climate variability in the Gulf*
759 *of Mexico* (No. 2011-3027). US Geological Survey.

760 Saunders, M. A., & Lea, A. S. (2008). Large contribution of sea surface warming to recent
761 increase in Atlantic hurricane activity. *Nature*, *451*(7178), 557-560.

762 Schaefer, K. M. (2001). Reproductive biology of tunas. *Fish Physiology*, *19*, 225-270.

763 Schmitz Jr, W. J., & McCartney, M. S. (1993). On the north Atlantic circulation. *Reviews of*
764 *Geophysics*, *31*(1), 29-49.

765 Seidov, D., Mishonov, A., & Parsons, R. (2021). Recent warming and decadal variability of
766 Gulf of Maine and Slope Water. *Limnology and Oceanography*, *66*(9), 3472-3488.

767 Sheinbaum, J., Candela, J., Badan, A., & Ochoa, J. (2002). Flow structure and transport in the
768 Yucatan Channel. *Geophysical Research Letters*, *29*(3), 10-1.

769 Trenberth, K. E., Cheng, L., Jacobs, P., Zhang, Y., & Fasullo, J. (2018). Hurricane Harvey
770 links to ocean heat content and climate change adaptation. *Earth's Future*, *6*(5), 730-744.

771 Volkov, D. L., Domingues, R., Meinen, C. S., Garcia, R., Baringer, M., Goni, G., & Smith,
772 R. H. (2020). Inferring Florida Current volume transport from satellite altimetry. *Journal*
773 *of Geophysical Research: Oceans*, *125*(12), e2020JC016763.

774 Wong, A. P., Wijffels, S. E., Riser, S. C., Pouliquen, S., Hosoda, S., Roemmich, D., ... &
775 Park, H. M. (2020). Argo data 1999–2019: two million temperature-salinity profiles and
776 subsurface velocity observations from a global array of profiling floats. *Frontiers in*
777 *Marine Science*, 700.

778 Wunsch, C. (2011). The decadal mean ocean circulation and Sverdrup balance. *Journal of*
779 *Marine Research*, *69*(2-3), 417-434.

780 Yu, L., Jin, X. and Weller, R. A. (2008). Multidecade Global Flux Datasets from the
781 Objectively Analyzed Air-sea Fluxes (OAFlux) Project: Latent and sensible heat fluxes,
782 ocean evaporation, and related surface meteorological variables. *OA-2008-1*, Woods Hole
783 Oceanographic Institution, 64 pp.

784 Zavala-Hidalgo, J., Pares-Sierra, A., & Ochoa, J. (2002). Seasonal variability of the
785 temperature and heat fluxes in the Gulf of Mexico. *Atmósfera*, *15*(2), 81-104.

786 Zavala-Hidalgo, J., Romero-Centeno, R., Mateos-Jasso, A., Morey, S. L., & Martínez-López,
787 B. (2014). The response of the Gulf of Mexico to wind and heat flux forcing: What has
788 been learned in recent years?. *Atmósfera*, *27*(3), 317-334.
789